RESEARCH ARTICLE

Editor's Choice

ADVANCED ENGINEERING MATERIALS

www.aem-journal.com

A High-Resolution Versatile Focused Ion Implantation Platform for Nanoscale Engineering

Mason Adshead, Maddison Coke, Gianfranco Aresta, Allen Bellew, Matija Lagator, Kexue Li, Yi Cui, Rongsheng Cai, Abdulwahab Almutawa, Sarah J. Haigh, Katie Moore, Nicholas Lockyer, Christopher M. Gourlay, and Richard J. Curry*

The ability to spatially control and modify material properties on the nanoscale, including within nanoscale objects themselves, is a fundamental requirement for the development of advanced nanotechnologies. The development of a platform for nanoscale advanced materials engineering (P-NAME) designed to meet this demand is demonstrated. P-NAME delivers a high-resolution focused ion beam system with a coincident scanning electron microscope and secondary electron detection of single-ion implantation events. The isotopic mass-resolution capability of the P-NAME system for a wide range of ion species is demonstrated, offering access to the implantation of isotopes that are vital for nanomaterials engineering and nanofunctionalization. The performance of the isotopic mass selection is independently validated using secondary ion mass spectrometry (SIMS) for a number of species implanted into intrinsic silicon. The SIMS results are shown to be in good agreement with dynamic ion implantation simulations, demonstrating the validity of this simulation approach. The wider performance capabilities of P-NAME, including sub-10 nm ion beam imaging resolution and the ability to perform direct-write ion beam doping and nanoscale ion lithography, are also demonstrated.

1. Introduction

Ion beam implantation is a critical technology that underpins the semiconductor industry.[1] With a drive toward miniaturization and the development of nanoscale materials and devices, there has been great interest in focused ion beam (FIB) technologies. FIB systems are capable of achieving nanoscale probe sizes, with depth and erosion rates tunable via ion beam current and energy variation. Such systems have found many applications across a variety of disciplines, largely due to their milling capabilities.[2] Examples include the milling of arrayed nanopores for multicolor generation;[3] microfabrication and failure analysis;[4] nanoscale device prototyping[5] (including Fresnel zone plates for high-resolution X-ray imaging);[6] localized materials engineering of electrochemically active systems;[7] and when in conjunction with other processes, the creation of plasmonic nanoparticles for single photon sources.[8] The use of FIB systems specifically for low-dose impurity-ion doping has been limited, though its potential is substantial with applications in developing fields such as quantum technologies. For example, when the FIB current is reduced to the point of a single-ion implantation, it becomes possible to deterministically create color centers for qubit array formation,[9–11] with control over dopant number and nanoscale positioning being crucial for device performance.[12,13] Such applications of ion implantation in quantum technologies often also demand the ability to deliver a variety of isotopically selected species for implantation in order to yield

M. Adshead, M. Coke, A. Almutawa, R. J. Curry
Department of Electrical and Electronic Engineering
Photon Science Institute
University of Manchester
Oxford Road, Manchester M13 9PL, UK
E-mail: mason.adshead@manchester.ac.uk

G. Aresta, A. Bellew
Ionoptika Ltd.
B6 Millbrook Close, Chandler's Ford, Hampshire SO53 4BZ, UK

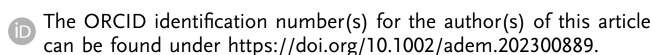
The ORCID identification number(s) for the author(s) of this article can be found under https://doi.org/10.1002/adem.202300889.

© 2023 The Authors. Advanced Engineering Materials published by Wiley-VCH GmbH. This is an open access article under the terms of the Creative Commons Attribution License, which permits use, distribution and reproduction in any medium, provided the original work is properly cited.

DOI: 10.1002/adem.202300889

M. Lagator, N. Lockyer
Department of Chemistry
Photon Science Institute
University of Manchester
Manchester M13 9PL, UK

K. Li, K. Moore
Department of Materials
Photon Science Institute
University of Manchester
Oxford Road, Manchester M13 9PL, UK

Y. Cui, C. M. Gourlay
Department of Materials
Imperial College London
London SW7 2AZ, UK

R. Cai, S. J. Haigh
Department of Materials
University of Manchester
Manchester M13 9PL, UK

optimal performance with regard to properties such as nuclear spin. This presents a challenge for FIB systems where the availability of different ions species from a common ion source and their isotopic selection has been restricted.

Liquid metal alloy ion sources (LMAISs) are able to deliver high-brightness ion beams for a variety of ion species, and are capable of sub-10 nm spatial resolution (beam spot-size), as measured by a 80% to 20% change in the intensity of the ion beam.[14] Beyond simple ion beam milling applications, high brightness LMAISs have been used for ion beam synthesis arising from their ability to dope materials via ion implantation at widely varying and highly localized doses, and to maintain stable low current operation for single ion implantation when implemented with some form of beam gating or chopping mechanism.[15] Detection of single ion implantation events has been achieved utilizing specific implantation targets including ion beam-induced charge (IBIC)[16] and avalanche[17] detectors, and even tests for photoluminescence between implantation events to determine whether or not an ion was successfully implanted.[18] Secondary electron detection of single ion implantation events provides a more convenient method of detection as it does not require any specific device architecture to be built into the implantation target.[19]

When a LMAIS is used in conjunction with an $E \times B$ filter (Wien filter), ion species present within the ion beam produced by the source may be separated based on their mass and charge state. Depending on the resolution of the filter, this can offer a range of ion species that can be isolated and implanted using a single source. A wide range of metal alloys have been explored with the aim of producing LMAISs.[20] However, some ion species require more complex alloys in order to achieve desirable source tip wetting conditions, which are often unable to be reliably reproduced, or suffer from source stability issues, and have only been studied for their emission properties without significant application in the field of device fabrication. The strong technological requirement for localized materials doping, with high spatial resolution and isotopic purity, has continued to prompt research into multiple methods of achieving this goal, including the work presented by Pacheco et al., which utilized IBIC detectors to measure the nanoscale precision of deterministic ion implantation with their FIB.[21] More recent approaches of deterministic ion implantation utilize systems such atomic force microscope (AFM) cantilevers in order to control the number of ions implanted and the spatial resolution of implantation, with up to 99.85% efficiency measured with IBIC detectors.[22] While such methods offer high deterministic implantation efficiencies, the ultimate scalability of the cantilever controlled implantation approach across an array of devices, or at wafer scale, is limited. A system capable of high-resolution implantation, which offers determinsitic capabilities, that is scalable over large areas within a reasonable time for implantation is urgently required to meet the nanoscale engineering requirements of emerging quantum technologies.

Here, we present a step improvement in the technological capability needed to achieve localized materials doping, demonstrated with the platform for nanoscale advanced materials engineering (P-NAME), the instrument that is shown in Figure S1, Supporting Information. P-NAME is an ion implantation tool capable of delivering maskless ion beam lithography and patterned doping using a FIB composed of isotopically selected ions from a variety of LMAISs. The system also has a coincident secondary electron microscope (SEM) to allow for nondestructive imaging and sample localization. Current applications being explored with the P-NAME tool include developing nanotechnologies such as solid-state impurity-ion and defect qubit devices (e.g., Sb in silicon,[23] color centers across a range of materials such as in diamond,[24–26] hexagonal boron nitride,[27,28] and also in silicon carbide[29,30]) and isotopic materials synthesis (and enrichment), the doping of nanoscale systems (e.g., Mn doping of epitaxial quantum dots and nanowires), ion beam lithography, doping of photonic waveguide structures (e.g., Er implanted into $LiNbO_3$[31]), and others.

In this work, we present the isotopic mass spectra of a range of LMAISs that have been developed for the P-NAME tool. We utilize time-of-flight secondary ion mass spectroscopy (ToF-SIMS) and nanoSIMS to independently validate the P-NAME mass selection performance through the analysis of silicon substrates doped with a variety of isotopically selected ion species. The ToF-SIMS data are utilized to corroborate simulations performed using the dynamic Monte Carlo ion implantation simulation package TRIDYN[32], providing further validation for the simulation package. We also demonstrate the wider performance of P-NAME including sub-10 nm ion beam imaging resolution and the ability to perform direct-write ion beam doping and lithography, and single ion implantation. These results certify the P-NAME system as a tool well suited for precision doping with high spatial accuracy and isotopic selection.

2. LMAISs

LMAISs are commonly used in FIB systems due in part to their high brightness and relatively low energy spread, ideally suited for applications requiring high spatial resolution (small spot size) at pA beam currents. Other sources utilized in FIB systems are typically designed for specific applications such as for high sputter yields for milling, high-resolution imaging, device editing and repair, etc. For a review on the ion sources for FIB systems, namely, inductively couple plasma, gas field ionization, and low temperature ion source, the interested reader is directed to the work by Smith et al.,[33] while an overview of LMAISs can be found in the work by Bischoff et al.[20] Other types of ion source offer some advantages over LMAISs, like sub-nm imaging resolution achievable in gas field ionization sources and high current milling capabilities in plasma sources. The ability of LMAISs to provide a wide variety of ion beam currents from a single source to facilitate high-resolution single ion implantation, as well as alloying and enrichment, makes these ideal sources for the P-NAME system.

The LMAISs used in this article were $Au_{73}Si_{14}Sb_{13}$, $Au_{78}Si_{12}Er_{10}$, $Au_{62}Ge_{28}Mn_{10}$, $Nd_{64}Co_{31}B_5$, $Bi_{57}Sn_{43}$, $Cu_{30}Nd_{70}$, and In. Some alloys were purchased prealloyed although all of these can now be produced in our laboratories starting with pure elements. For alloys consisting of only Bi, Sn, and/or In, LMAIS fabrication involved resistance melting of elemental mixtures in graphite. For other alloys, multistep arc melting of mixed elements on a water-cooled copper hearth was applied. Alloys were then fabricated into ion sources by melting the alloy in a crucible

© 2023 The Authors. Advanced Engineering Materials published by Wiley-VCH GmbH

15272648, 0, Downloaded from https://onlinelibrary.wiley.com/doi/10.1002/adem.202300889 by Imperial College London, Wiley Online Library on [29/09/2023]. See the Terms and Conditions (https://onlinelibrary.wiley.com/terms-and-conditions) on Wiley Online Library for rules of use; OA articles are governed by the applicable Creative Commons License

and dipping the prepared element coil into the liquid metal, before being withdrawn and allowed to cool. Tests were then performed to ensure source ignition and stable emission prior to installation into the P-NAME system.

The LMAISs developed have a typical coiled reservoir of alloyed metal, which is resistively heated to a sufficient melting point in order to flow down, and ultimately wet, the tip of the source. As is typical in LMAIS modules, there is both an extractor and suppressor unit which are used to generate and stabilize emission from a fully wet tip, respectively,[34] with a maximum acceleration voltage for the ions in the P-NAME system being 25 kV. At such energies, the implanted ions are typically confined to the top 100 nm or so from the substrate surface, with additional growth on top of the implanted surface achievable with standard deposition systems to create a deeper buried implantation layer, if desired.

The LMAIS utilized in this study have all exhibited stable emission, with ion beam current variation being typically <0.1% over many hours of use. The lifetimes of these sources vary from alloy to alloy, with sources achieving over 2000 μAh of emission. The ranges in ion beam dose that these sources have delivered in the P-NAME system range from single ion implantation to $>10^{20}$ ions cm^{-2}.

3. System Overview and Ion Beam Lithography

The P-NAMEs maximum anode voltage of 25 kV allow in ion implantation energies typically from <5 to 75 keV depending on the charge state (and whether there is clustering) of the particular ion species selected from the LMAIS. The system also has a coincident SEM enabling high-resolution imaging of samples and devices without prior exposure to the ion beam, facilitating nondestructive targeting with nanoscale accuracy. The ion column is fitted with a neutral mass filter to ensure that only the selected ion species is implanted into the sample or device. The stage of the P-NAME system has nanometer positioning control using piezocontrollers, and supports a sample platen capable of receiving up to a 6 inch wafer. The platen has a fixed 3° ion beam offset to reduce ion channeling during implantation. The maximum ion beam write area (field of view) at 25 kV is $610 \times 610\,\mu m^2$ and increases with decreasing anode voltage to $850 \times 850\,\mu m^2$ at 5 kV, where the write area becomes aperture limited. The doping of patterns and structures exceeding these dimensions is afforded by tiling using the platen positioning control. Samples are introduced via a vacuum gated load-lock ensuring the main chamber remains under vacuum with a base pressure of $\approx 3 \times 10^{-9}$ mbar. The sample handling capabilities of the system enable vacuum suitcase attachment and sample transfer, allowing samples to be transferred between the P-NAME system and deposition systems without breaking vacuum at any stage, facilitating the investigation of modified interfaces.

An example of the imaging resolution achievable with the P-NAME system is provided in **Figure 1**. The secondary electron image of tin nanospheres on a carbon substrate was obtained using a 25 kV Bi^{2+} ion beam (Figure 1a). The resulting beam resolution was determined using the 80/20 knife-edge measurement of a linescan across a sharp change in contrast. The system was able to achieve a measured imaging resolution of 6.8 (±1.4) nm (Figure S2, Supporting Information). Figure 1b shows a typical coincident 25 kV SEM image of tin nanospheres on the same standard. The image has been processed by the SEM acquisition software to partially correct for the imaging angle deviation of the electron beam (54°) from the near-normal ion beam.

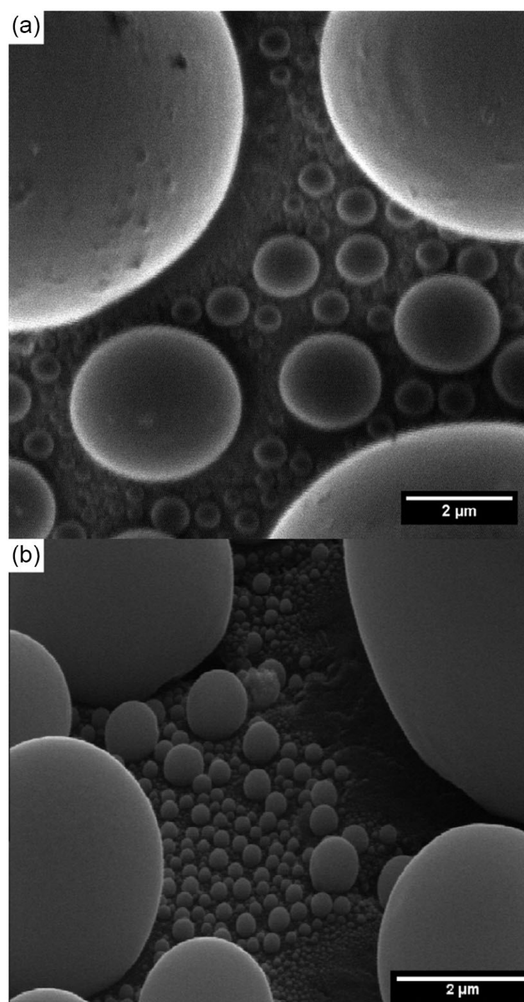

Figure 1. Demonstration of the imaging capabilities using the P-NAME system. a) Ion beam image of Sn nanospheres on carbon displaying sub-10 nm resolution obtained using secondary electron detection with a 25 kV Bi^{2+} beam (260 ± 38 fA beam current measured in the sample space). Resolution was measured using the 80/20 knife-edge method. b) Secondary electron image formed by the coincident SEM image of Sn nanospheres, which enables nondestructive implantation site localization with submicron accuracy.

The P-NAME ion column has high-frequency beam blanking capability that enables <100 ns ion beam pulses while also being able to operate in continuous beam exposure mode. This allows maskless direct-write doping and lithographic patterning when coupled with control over ion beam positioning. This versatility enables the system to be readily used across a variety of materials and devices for rapid prototyping of new technologies, especially where high spatial resolution (sub-10 nm beam size) is vital.[35] **Figure 2** shows AFM images of the results of ion beam lithography using polymethyl methacrylate (PMMA) resist, exposed to a

© 2023 The Authors. Advanced Engineering Materials published by Wiley-VCH GmbH

15272648, 0, Downloaded from https://onlinelibrary.wiley.com/doi/10.1002/adem.202300889 by Imperial College London, Wiley Online Library on [29/09/2023]. See the Terms and Conditions (https://onlinelibrary.wiley.com/terms-and-conditions) on Wiley Online Library for rules of use; OA articles are governed by the applicable Creative Commons License

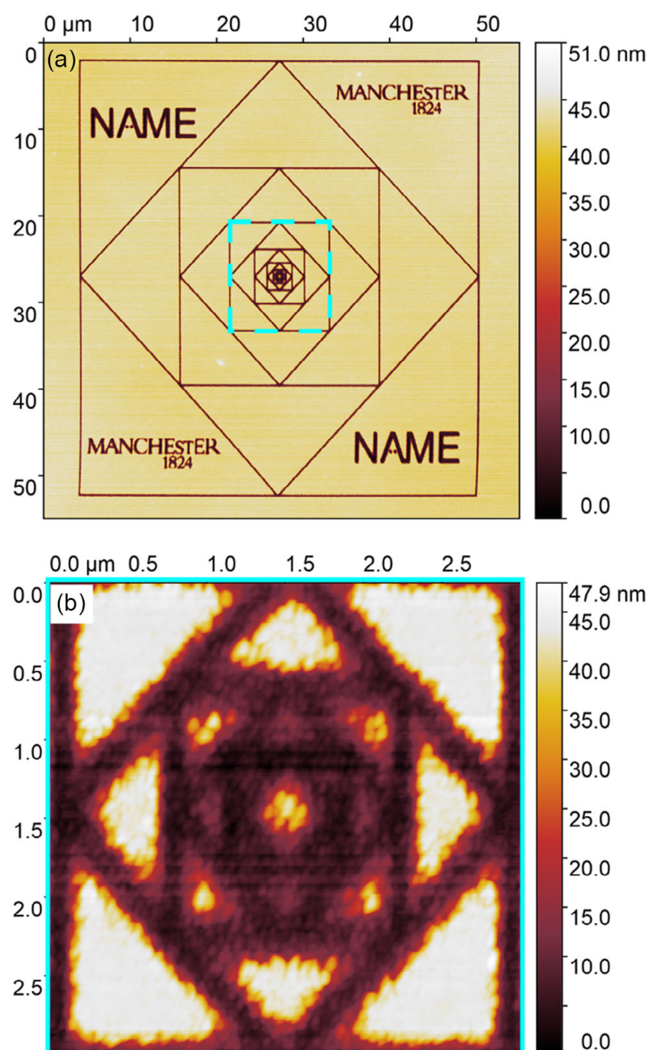

Figure 2. AFM images of the of ion beam lithographic patterns produced using 25 kV Au^+ ions exposing PMMA resist at a dose of 1×10^{13} ions cm^{-2}. a) Full pattern showing alternating concentric squares and included round edge designs. b) 3 μm field of view image of the center-most structures. The inner-most rotated square is distinguishable with lengths on the order of 500 nm, despite the inhomogeneity of exposure beyond the directly ion beam implanted regions at this scale.

25 kV Au^+ beam with a dose of 1×10^{13} ions cm^{-2} and a beam spot-size of 52.5 (±9.1) nm.

Figure 2a shows the full exposed pattern of 14 alternating rotated concentric squares. The patterns within the large spaces further demonstrate the lithographic capabilities in both straight lines, with sharp angles, and rounded edges, the quality of which are key for the development of a variety of structures in metasurfaces, for example.[36] Figure 2b shows a 3×3 μm^2 AFM scan of the very center of the lithography pattern in Figure 2a, where the smallest of the squares (a rotated square with side lengths on the order of 500 nm) is distinguishable. At such scales, it is clear that the PMMA exposure due to the Au^+ ion beam is inhomogeneous, with the main area of exposure being confined to the approximately 122 nm width of the lines as per the design. Nonetheless, there is some exposure which extends beyond this, possibly due to ion straggle and electronic damage causing resist exposure outside of the region of direct ion implantation.

A further demonstration of the ion beam write control of the P-NAME system is presented in **Figure 3**. An AFM image of a subset of an array of 128×128 point exposures, each separated

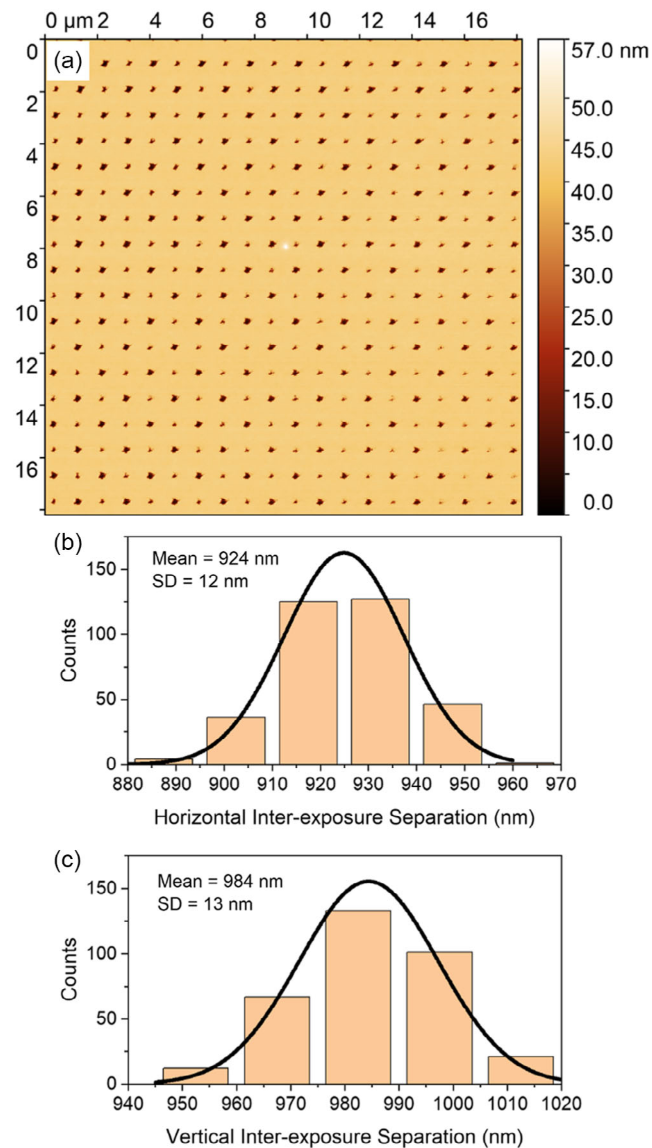

Figure 3. Demonstration of the capability of the P-NAME system to deliver arrays of implanted ions of varying dose. a) AFM image of an 18×20 sub-array obtained from within an array of 128×128 point exposures, with consistent separation between the pixels. The white feature near the center of the image is minor contamination on the surface of the sample. The doses of the points were varied in an alternating manner in the top left to bottom right diagonal, between a varying dose exposure (from 3×10^{11} ions cm^{-2} to 1×10^{13} ions cm^{-2}), with a fixed dose of 1×10^{13} ions cm^{-2}. The larger points in the imaged sub-array correspond to the higher dose exposure. b) Histogram of the horizontal inter-exposure separation, fitted with a Gaussian (black line). c) Histogram of the vertical inter-exposure separation, fitted with a Gaussian (black line). Standard deviations (SD) of the mean separations are given.

© 2023 The Authors. Advanced Engineering Materials published by Wiley-VCH GmbH

15272648, 0, Downloaded from https://onlinelibrary.wiley.com/doi/10.1002/adem.202300889 by Imperial College London, Wiley Online Library on [29/09/2023]. See the Terms and Conditions (https://onlinelibrary.wiley.com/terms-and-conditions) on Wiley Online Library for rules of use; OA articles are governed by the applicable Creative Commons License

by consistent spacing, is shown in Figure 3a. Each point exposure was performed using 25 kV Au^+ ions into PMMA on silicon. The dose of the exposed points was kept constant along each diagonal line of points extending from the top right to bottom left, with the specific doses of these lines alternating between a fixed reference dose (1×10^{13} ions cm^{-2}) and a varied dose, decreasing from 1×10^{13} ions cm^{-2} to 3×10^{11} ions cm^{-2} from the top left to bottom right corner of the image. The size and shape of the individual exposures directly correlates to the ion dose, with the higher dose exposures resulting in larger features. Analysis of the interexposure spacings provides a mean separation of 924 ($\pm$12) nm and 984 ($\pm$13) nm for the horizontal and vertical separations, respectively. The histograms of the horizontal and vertical separations are shown in Figure 3b,c, respectively. This, along with Figure 2, demonstrates excellent precision and reproducibility of the ion beam exposure control, with exposures of the PMMA only occurring at the intended locations.

The stable low emission current from the LMAIS allows the P-NAME system to utilize its rapid ion beam blanking control in order to deliver single ion implantation. This capability, coupled with the in-chamber secondary electron detectors, facilitates deterministic implantation. The dark-count value (false-positive detection rate) of the secondary electron detectors in the P-NAME system is $\approx 8 \times 10^{-6}$ per typical 1 μs pulse. As shown by Murdin et al., at such a low dark-count rate, the ability to perform single-ion deterministic doping is limited solely by the ion implantation detection efficiency[10] which, for P-NAME, was measured in the same manner as Cassidy et al.,[37] to be 87 ($\pm$7)% for 50 keV Sb into 200 nm SiO_2 on p-type (boron doped) Si (see Figure S3, Supporting Information). For measuring the detection efficiency, the average number of ions within a given pulse (λ) was varied by adjusting the pulse width for a fixed ion beam current. The beam pulsed 2000 times for each λ, with the number of successful detections (those resulting in a corresponding secondary electron signal) recorded. Detection signals corresponding to individual pulses for $\lambda = 0.06$ are shown in **Figure 4**. The orange trace shows the detection signal from an implantation event with the rise time and decay governed by the detection electronics. Rarely, multiple events are observed as shown by the black trace. It is believed that these two traces correspond to a single and double implantation events, respectively, resulting from the Poissonian nature of the beam.

A demonstration of the single ion implantation capability of the P-NAME system in nondeterministic mode (implanting without secondary electron detection) is shown in **Figure 5**, where high-angle annular dark field scanning transmission electron microscope (HAADF-STEM) images are presented. Here, a 20 nm-thick Si membrane was implanted with 15 keV $^{123}Sb^+$ ions. The beam was rastered over an area of 153.6×122.88 μm², achieved by moving the sample stage and tiling together various 15.36×15.36 μm² exposures, each composed of 512×512 pixels, resulting in a 30 nm separation between each point in the exposure. The low current ion beam (200 fA) was exposed for a short period of time (800 ns), such that each point of exposure had a 37% probability of having one ion ($\lambda = 1$, with the number of ions in a given point exposure following Poissonian statistics).

The Z-contrast HAADF-STEM image in Figure 5a shows a small region of the implanted membrane, with the Sb ions appearing as bright spots (locations highlighted orange dashed circles) due to their higher atomic number than the Si substrate. Higher magnification images of the locations of the Sb ions are shown in Figure 5b,c, with Figure 5b showing a pair of Sb ions, with an intensity linescan across this pair revealing the high intensity peaks containing Sb relative to the pure Si atomic columns (linescan inset in Figure 5a). The Sb ions were overwhelmingly located on a Si lattice site (Figure 5c), suggesting the Sb ion has been incorporated into the Si crystal lattice despite no dedicated postimplantation annealing having been applied.

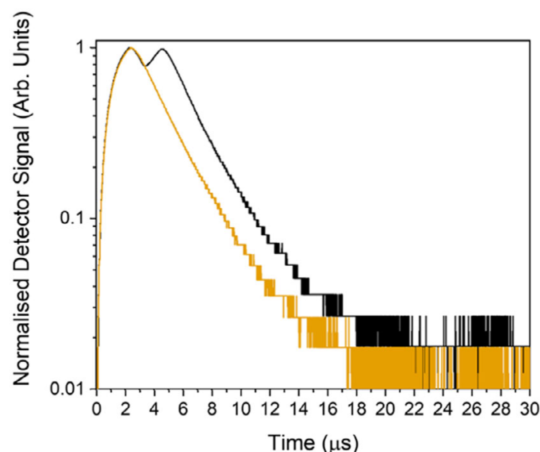

Figure 4. Secondary electron detector signals resulting from the implantation of a pulsed ion beam, with a 600 ns pulse ($\lambda = 0.06$ ions per pulse). The orange signal has a single peak, while the black signal has two peaks. This is believed to correlate to the number of ions within a given pulse due to Poissonian statistics; single ion implantation event detected in the orange signal, and two independent ion implantation events observed in the black signal, both from independent pulses of the ion beam.

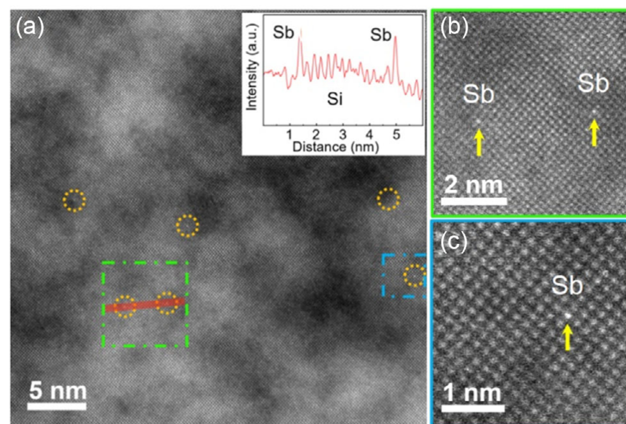

Figure 5. HAADF-STEM Z-contrast images of a 20 nm thick Si membrane, implanted with 15 kV $^{123}Sb^+$ ions. The implantations were achieved using a pulsed beam with an average of one ion per pulse, and a set separation of 30 nm. a) Image showing multiple identified Sb ions in the Si membrane (orange dashed circles), with the red line indicating the intensity linescan shown in the inset. b) Magnified view of the two Sb ions from the region of the green box in (a), with yellow arrows indicating the locations of Sb ions. c) Magnified view of a single implanted Sb ion from the region of the blue box in (a), with a yellow arrow indicating the Sb ion.

© 2023 The Authors. Advanced Engineering Materials published by Wiley-VCH GmbH

15272648, 0, Downloaded from https://onlinelibrary.wiley.com/doi/10.1002/adem.202300889 by Imperial College London, Wiley Online Library on [29/09/2023]. See the Terms and Conditions (https://onlinelibrary.wiley.com/terms-and-conditions) on Wiley Online Library for rules of use; OA articles are governed by the applicable Creative Commons License

The separation of the implanted ions is also of interest, with the ions in Figure 5b being separated by approximately 3.5 nm, much less than the 30 nm separation of implantation events during exposure. This close proximity could either be due to a double implantation due to Poissonian statistics (probability of a pulse containing more than one ion for this particular ion beam configuration was ≈26%), or possibly a single implantation event of an ion cluster due to the doubly charged Sb cluster isobar in the ion beam (discussed below). This is only a proof of principle demonstration and future investigations will include quantification of the single ion implantation over larger areas and incorporating secondary electron detection into such an experiment with a small λ, in order to ensure each site is implanted and to suppress the probability of having a pulse containing more than one ion.

The single ion implantation capability, with the possibility of deterministic control over the quantity of ions implanted, allows the system to be utilized towards the realization quantum technologies, e.g., qubit devices, where the control of the number of ions, as well as their location, is of great importance. The P-NAME tool offers the additional advantage of isotopic selection of these ions, discussed below, enabling selection or exclusion of specific nuclear spin isotopes.

4. Isotopic Mass Selection

The mass selection capability of the ion column is realized via the use of a standard in-column E × B (Wien) filter. The Wien filter uses a fixed magnetic field and variable electrostatic plate voltage, V_{WF}. Conversion of V_{WF} to the selected ion mass, m, is given by

$$m = \frac{V_{\mathrm{acc}} q}{2\left(\frac{V_{\mathrm{WF}}}{\delta B}\right)^2}(1000 N_{\mathrm{A}}) \tag{1}$$

where V_{acc} is the ion acceleration voltage, q is the charge of the ion species (in terms of the universal electronic charge (e_{c})), δ is the electrostatic plate separation, and B is a fitting parameter that correlates to the permanent magnetic field strength of the Wien filter. The term $1000N_{\mathrm{A}}$ converts the mass from kg to atomic mass unit (amu), with N_{A} being Avogadro's constant.

Measuring the ion beam current in the sample chamber (via a Faraday cup) as a function of V_{WF} provides an ion beam current spectrum that may be converted into a mass spectrum using Equation (1). The inclusion of a variable beam aperture allows the mass resolution to be tuned, with the mass resolving power, R, of the system described by

$$R = \frac{m}{\Delta m} = \frac{qBL\left(S + \frac{L}{2}\right)}{2d\sqrt{2V_{\mathrm{acc}} q \frac{m}{1000N_{\mathrm{A}}}}} \tag{2}$$

where Δm is the full-width-half-maximum (FWHM) of the resulting mass spectrum peak, L is the length of the electrostatic plates, S is the drift distance between the end of the electrostatic plates and the mass resolving aperture, and d is the diameter of the mass resolving aperture. It is clear that the use of a smaller aperture increases the resolution of the isotopic mass peaks, as demonstrated in **Figure 6**. The key factors that affect the performance of the Wien filter are the mass resolving aperture diameter, and the drift distance, both resulting in a small selection angle of the ion beam. This small selection angle means that even with narrow separation in beam spread due to the mass–charge ratio of the ions in the beam coming out of the electric and magnetic crossed-field region, these beams can still be selectively tuned to pass through the mass resolving aperture with isotopic resolution (selecting one to pass through, while the others are blocked).

Wien filter mass spectra for mono- and multi-isotopic species obtained using sources developed for the P-NAME tool are presented in **Figure 7**. In order of atomic mass, these are B, Si, Mn, Co, Cu, Ge, In, Sn, Sb, Nd, Er, Au, and Bi. All of the spectra displayed in Figure 7 were obtained using an accelerating voltage of 25 kV and a mass resolving aperture of 50 μm diameter, with the exception of boron which was obtained without a mass resolving aperture due to a relatively low beam current. It is clear from Figure 7a, however, that even without the aid of a mass resolving aperture the B^+ isotopes are fully resolved.

The Wien filter mass spectrum of silicon is shown in Figure 7b with each isotope fully resolved and the Si^{2+} ion current intensity being ≈6 times that of the Si^+ intensity. This is noteworthy as it enables the tool to perform isotopic doping of ^{28}Si at an energy of up to 50 keV using the doubly charged species at the maximum acceleration voltage.

The Wien filter mass spectra of manganese and all the other monoisotopic species (cobalt, gold, and bismuth) are collated into a single spectrum (Figure 7c). This does not indicate that these species originate from the same LMAIS. It is noted that the singly charged ion current dominates over the doubly charged ion current for Au and Bi, while it is comparable for Co. Only singly charged Mn was measured from the source used to obtain this part of the spectrum. The inset of Figure 7c shows an optical

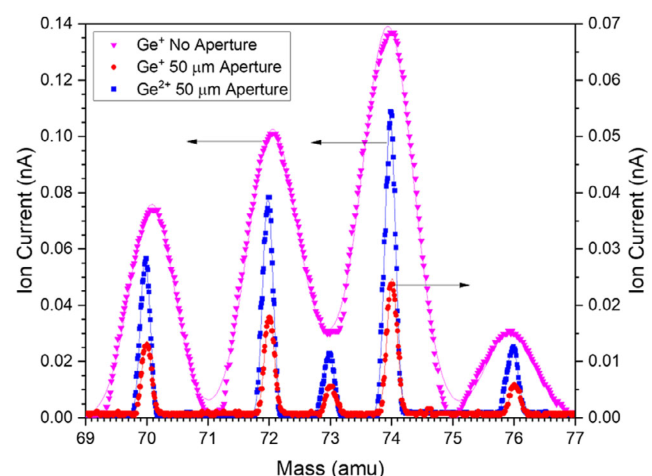

Figure 6. Demonstration of the tunability of the Wien filter mass resolution with 25 kV Ge^+ isotopes. Without an aperture (pink inverted triangles), the $^{73}Ge^+$ isotope cannot be resolved from its neighboring peaks. However, using a 50 μm aperture (red circles) all the isotopes are resolved, albeit with a reduction in beam current. A scan of Ge^{2+}, also with a 50 μm aperture, is included for comparison. Each isotope in the resolved spectra is fitted with a single-peak Gaussian, while the unresolved spectrum is best fit with a five-peak Gaussian.

© 2023 The Authors. Advanced Engineering Materials published by Wiley-VCH GmbH

15272648, 0, Downloaded from https://onlinelibrary.wiley.com/doi/10.1002/adem.202300889 by Imperial College London, Wiley Online Library on [29/09/2023]. See the Terms and Conditions (https://onlinelibrary.wiley.com/terms-and-conditions) on Wiley Online Library for rules of use; OA articles are governed by the applicable Creative Commons License

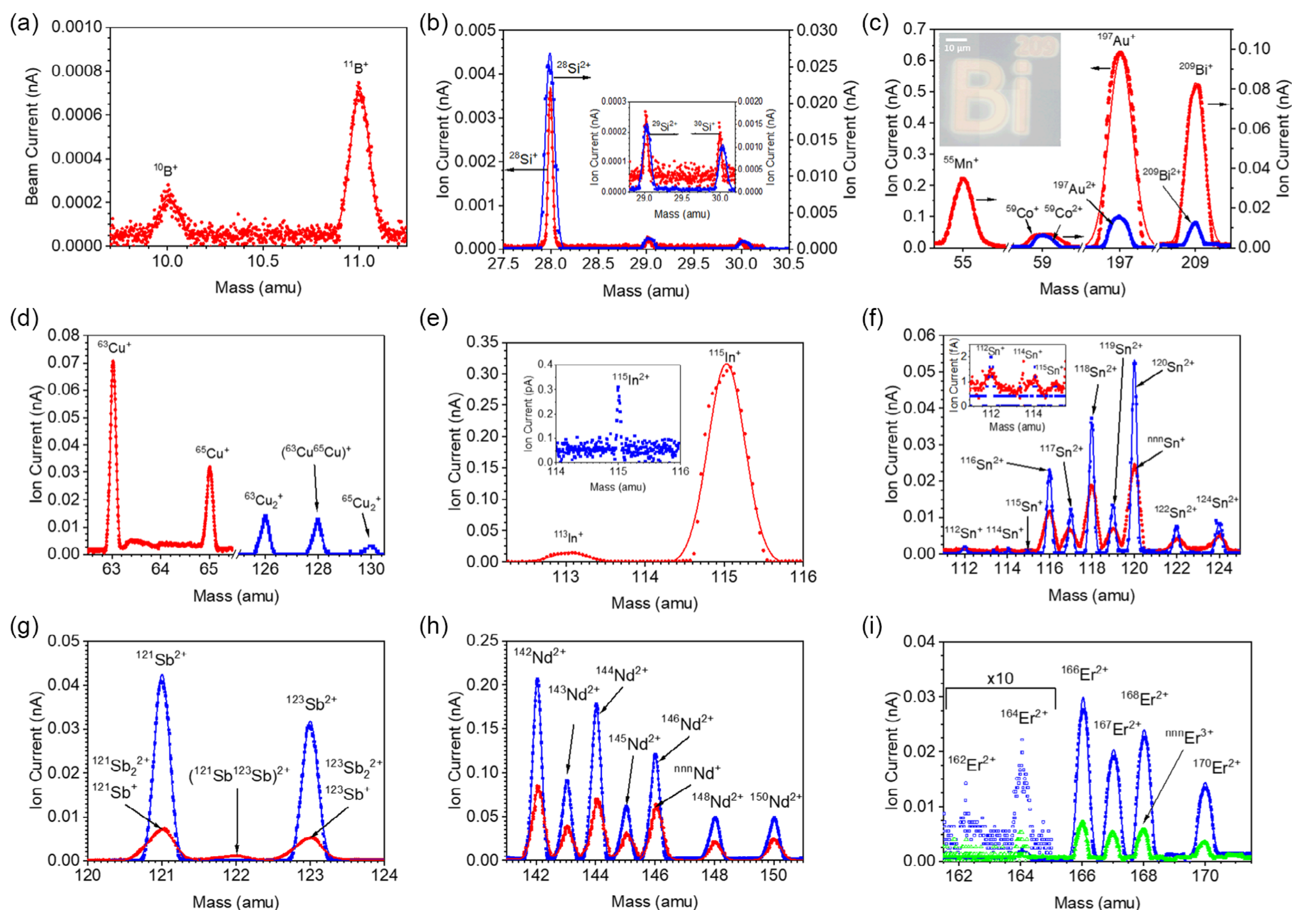

Figure 7. Wien filter mass spectra of the ion species accessible from the LMAISs so far utilized in the P-NAME system. All spectra were obtained by varying the voltage of the Wien filter electrostatic plates, with Equation (1) being used to calibrate the mass of the isotopes. All spectra were obtained using a 25 kV acceleration voltage and, with the exception of B^+, a 50 μm mass resolving aperture. The panels shown provide data for the isotopes of a) B, and b) Si (with lower mass isotopes magnified in the inset), c) the mono-isotopic ions of Co, Mn, Au, and Bi (with an optical microscope image of Bi-209 label implanted into Si using a ^{209}Bi isotope ion beam shown in the inset), and the isotopes of d) Cu, e) In (with doubly charged species in the inset), f) Sn (with magnification of low current isotopes in the inset), g) Sb, h) Nd, and i) Er. In all panels, red circles, blue squares, and green triangles indicate singly-, doubly-, and triply-charged ions, respectively. In (i), hollow versions of the symbols indicate a magnification of the datapoints. In all spectra, with the exception of the magnified datapoints in (i) and the In^{2+} spectrum inset in (e), the peaks are presented with Gaussian fits used to perform peak analysis (see text for details).

microscope image of a direct-written Bi-209 label, doped into silicon using the ^{209}Bi isotope.

Copper has two stable isotopes, ^{63}Cu and ^{65}Cu, both of which are fully resolved in Figure 7d. Also, present in the Wien filter spectrum in Figure 7d are isotopic cluster variations of $(Cu_2)^+$ in addition to a third peak arising from the mixed isotope cluster $(^{63}Cu^{65}Cu)^+$. Indium, like Cu, has two stable isotopes which are resolved in Figure 7e, and the doubly charged species is present, albeit with a significantly reduced beam current (inset in Figure 7e), demonstrating that the principal mode of emission for In is as a singly charged ion.

Tin has the greatest number of stable isotopes (ten) all of which we are able to be resolved and can be observed in both charge states (Figure 7f). The doubly charged ion current is found to be twice that of the singly charged ion current and allows for full mass separation due to the increased resolving power the additional charge provides (Equation (2)). Figure 7g shows the Wien filter mass spectrum for antimony where again the doubly charged ion has a higher current and affords full mass separation. Also, present within the spectrum is a peak corresponding to the mixed isotope cluster $(^{121}Sb^{123}Sb)^{2+}$ which implies the presence of the doubly charged isotopic clusters ($^{121}Sb_2^{2+}$ and $^{123}Sb_2^{2+}$). These are isobars of the singly charged single-ion isotopes, and so the peaks overlap within the spectrum. This has important implications for single ion implantation since on selecting a single isotope of Sb^+, it is possible that a cluster is, instead, implanted (see discussion of Sb ion from the STEM images in Figure 5).

The Wien filter mass spectrum of neodymium is shown in Figure 7h, resolving the five stable isotopes and two long-lived radioisotopes (^{144}Nd and ^{150}Nd). The doubly charged ion current was approximately twice that of the singly charged ions. For erbium, the six stable isotopes can be resolved for the doubly charged ions (Figure 7i); however, the reduction in beam current

 © 2023 The Authors. Advanced Engineering Materials published by Wiley-VCH GmbH

15272648, 0, Downloaded from https://onlinelibrary.wiley.com/doi/10.1002/adem.202300889 by Imperial College London, Wiley Online Library on [29/09/2023]. See the Terms and Conditions (https://onlinelibrary.wiley.com/terms-and-conditions) on Wiley Online Library for rules of use; OA articles are governed by the applicable Creative Commons License

for the triply charged ions leads to only five clearly visible isotopes. Though ^{162}Er is present (it is possible to produce a weak secondary electron image), the current is too small to be measured by the method used for the collection of this spectrum.

Within the above-described Wien filter mass spectra, a number of high mass clusters have been identified. We note that, in addition to these, other multispecies ion clusters can be found during wider scan ranges depending on the elemental composition of the LMAIS utilized. The identification of such clusters is beyond the scope of this article, and the reader is directed to Bischoff et al.[20] for an idea of the range of clusters available from a variety of LMAISs.

The degree of mass resolution, R, that is achievable with the P-NAME system is calculated according to Equation (2) and tabulated in **Table 1**. In all cases, the value of R is such that it is possible to obtain the natural isotopic abundance via integration and comparison of the relative areas under the isotopic peaks. These are tabulated in Table S1, Supporting Information, alongside the reported natural abundance.

The resolving power figures in Table 1 were obtained by fitting Gaussian profiles to the peaks of each isotope in the spectra depicted in Figure 7. The peak position and FWHM of the Gaussian fit are m and Δm, respectively, from which R was obtained. It is important to note that the P-NAME resolving powers provided in Table 1 are representative in that the figures stated were obtained using a 50 μm beam aperture. However, higher mass resolving powers are obtainable with smaller apertures as per Equation (2), albeit with the cost of reduced beam current.

These resolving powers represent among the highest achieved for a FIB system across a range of ion sources, compared with those reported both in the literature and in commercially available systems. Table 1 compares our results with resolving powers from Wien filter scans available in the literature, where unless otherwise specified, the mass-resolution values from reported literature data were derived via digitization of spectra presented in the cited sources (see Experimental Section for more detail). The same Gaussian fitting as described above was then used to obtain R for the digitized data.

The P-NAME tool is configured to provide high-quality isotopic separation of Si which leads to the highest resolving power ($R = 560$) for the singly charged species, which significantly outperforms other reported systems.[20,38–47] The instrument also provides sufficient separation of the doubly charged Si isotopes with a lower value of R, enabling the higher ion current to be taken advantage of. The lowest resolving power is obtained for B^+ ($R = 90$) which is still sufficient to resolve both isotopes, though in this case no mass resolving aperture was utilized due to the low ion current. For all other ion species reported in Table 1, the P-NAME system outperforms the reported literature values for similar FIB tools. Specialist ion implantation facilities are able to deliver higher mass resolution, though without the versatile capabilities afforded by FIB tools.

Table 1. Mass-resolution values of the P-NAME system (Figure 7, average of all isotopes), compared to those in the literature.

Species available	P-NAME resolving power (representative), R	Literature resolving power (indicative)[a)], R
B^+	90 (±2)	154[20]
Si^+	560 (±15)	288,[20] **20–40**,[38] 20,[39] 80,[40] 100,[41] 150[42]
Si^{2+}	263 (±3)	296,[40] **20–40**,[38] 13,[39] 156,[40] 173,[41] 146[42]
Mn^+	367 (±1)	70[20]
Co^+	124 (±2)	124[20]
Co^{2+}	205 (±3)	95[20]
$(Cu_2)^+$	351 (±6)	123[43]
Cu^+	469 (±2)	411[44]
Ge^+	387 (±3)	70,[20] 60,[20] 20,[41] **70**[43]
Ge^{2+}	365 (±2)	180,[20] 130[41]
In^+	215 (±5)	30[20]
Sn^+	190 (±12)	178[20]
Sn^{2+}	496 (±34)	412,[20] 479[20]
Sb^+	296 (±7)	112[20]
Sb^{2+}	500 (±2)	295[20]
Nd^+	320 (±3)	60[20]
Nd^{2+}	404 (±2)	56[20]
Er^{2+}	371 (±11)	50,[45] 20[45]
Er^{3+}	526 (±12)	130[45]
Au^+	245 (±2)	186,[20] 10,[38] 10,[39] 40,[40] 60,[20] 30,[41] 70[42]
Au^{2+}	363 (±2)	191,[20] 10,[38] 10,[39] 70,[40] 70,[20] 50,[41] 100[42]
Bi^+	123 (±1)	80,[46] 70,[46] 40,[46] 100,[46] 10[47]
Bi^{2+}	217 (±1)	50,[46] 120,[46] 70,[46] 90,[46] 10[47]

[a)]Values obtained from the cited reference via digitization (see Experimental Section for details). Bold values are taken directly as provided in the cited reference. In all cases, the cited reference relates to a FIB system.

Figure 8 presents the calculated abundance of each isotope detected in the P-NAME ion beams and compares this to the reported natural abundance.[48] Excellent agreement is found across the higher percentage abundances; however, the lower percentage values (particularly $<1\%$) differ more from the literature value. This is likely due to the signal-to-noise ratio of the ion beam current measured in the P-NAME system. While such strong agreement is expected for nonradioisotope sources, it is feasible that a similar system could be developed in order to perform precision radioisotope doping of materials in the future.

5. Verification of Isotopic Purity

To verify the isotopic selection capability of the P-NAME tool, a series of test implantations were undertaken for subsequent postdoping analysis. **Figure 9** provides SIMS analysis of various implanted species into intrinsic (previously undoped) silicon.

Figure 9a–d show results from ToF-SIMS. A 40 keV C_{60}^+ ion beam was used to sputter the substrate to obtain a stream of secondary ions which were then detected, in positive ion mode, to form a 2D map of a particular isotope. Several of these maps were

© 2023 The Authors. Advanced Engineering Materials published by Wiley-VCH GmbH

15272648, 0, Downloaded from https://onlinelibrary.wiley.com/doi/10.1002/adem.202300889 by Imperial College London, Wiley Online Library on [29/09/2023]. See the Terms and Conditions (https://onlinelibrary.wiley.com/terms-and-conditions) on Wiley Online Library for rules of use; OA articles are governed by the applicable Creative Commons License

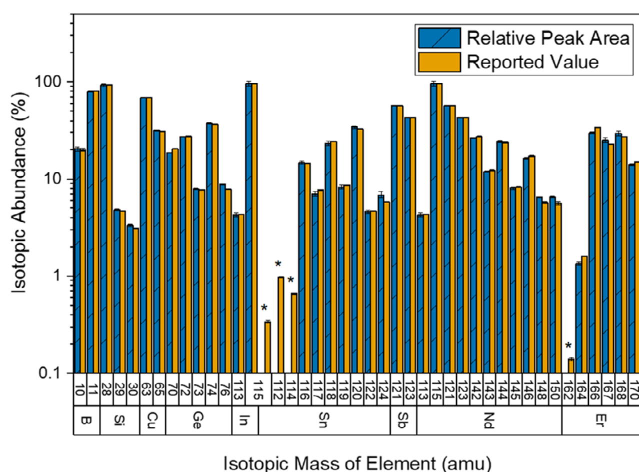

Figure 8. Comparison of isotopic abundances of the multi-isotopic elements from the spectra shown in Figure 7 with previously reported values (orange bars).[48] The calculated values (blue hatched bars) result from the area under the peak of a specific isotope relative to the total area under the peaks of all the isotopes of the element. For each case, the higher current spectrum was chosen. The abundances are plotted on a log axis in order to better visualize the isotopes with lower abundance. The relative peak area values for isotopes below 1% (marked with an * in the figure) are not plotted (or tabulated in the *R* value data Table S1, Supporting Information) due to a high signal-to-noise ratio for these isotopes, leading to too great an uncertainty in their measured area.

obtained on subsequent sputtered layers, corresponding to an analyzed depth. These layers were given a false color for each isotope, and all the layers summed to provide the single 2D datastacks shown in Figure 9a,d.

Figure 9a shows the integrated ToF-SIMS signal of a series of $5 \times 5\,\mu m^2$ squares of Cu^+ and Nd^+ isotopes implanted into an intrinsic Si substrate. Each column was doped with a different isotope, with slight variations in specific dose of implantation, which are, from left to right, ^{146}Nd (4.38×10^{16} ions cm^{-2}), ^{144}Nd (3.93×10^{16} ions cm^{-2}), ^{142}Nd (3.93×10^{16} ions cm^{-2}), ^{65}Cu (3.93×10^{16} ions cm^{-2}), and ^{63}Cu (5.77×10^{16} ions cm^{-2}). To detect the spatial distribution of implanted ions, the C_{60} analysis beam in the ToF-SIMS was rastered over a $100 \times 100\,\mu m^2$ area encompassing the entire implanted region, using a dose of 1×10^{14} ions cm^{-2} for each layer. The lateral beam step resolution was 400 nm and the C_{60} beam diameter was $\approx$500 nm. The apparent misalignment of the implanted squares is an artifact of the ToF-SIMS analysis, as the sample stage of the SIMS instrument drifted during the acquisition. A linescan across the top row of isotopes in Figure 9a is provided in Figure 9b, presented using a log-scale. It can be seen that the intensity measured for each implanted Nd isotopic dose is fairly consistent across the scan. For Cu, the intensity of the ^{65}Cu is less than that of the ^{63}Cu isotope, which reflects the variation in ion implantation dose for these isotopes (visually exaggerated, due to the logarithmic plot of the intensity). The general difference in intensity of the SIMS signal between the Nd and Cu present in the linescan in Figure 9b is likely due to variation in the SIMS relative sensitivity factors of the two elements, though such data for C_{60} sources in the literature are sparse.

Each doped region is spatially identifiable with an order of magnitude drop in concentration of implanted species found to occur within the first 1.5 μm from the implanted edge. A further order of magnitude reduction is then observed over 2.7 μm from the implanted edge. This indicates an extended tail in the low-current extremes of the presumed Gaussian profile of the doping ion beam, as may be expected from a LMAIS according to the literature.[49]

Figure 9c shows a depth profile of the various Cu and Nd isotopes obtained from the ToF-SIMS analysis, with the doses for each indicated above (in units of $\times 10^{16}$ ions cm^{-2}). Depth calibration of the ToF-SIMS was performed using AFM of the resulting sputtered crater (measured to be 59 nm, see Supporting Information, Figure S4). It is assumed that the amorphized implanted Si region had a constant ToF-SIMS etch rate. Previous work has shown that for higher doses of heavy ion species, the dynamic Monte Carlo simulation package TRIDYN is more accurate in predicting ion implantation profiles than the nondynamic code on which it is based (Stopping and Ranges of Ions in Matter, aka SRIM).[50] For this reason, TRIDYN was used to simulate the ion implantation of Cu^+ and Nd^+ into Si. A good agreement between the TRIDYN model and ToF-SIMS data was found (Figure 9c), providing evidence for the validity of the simulation package at the doses used for these implantation studies. The Nd isotope data agree consistently with the TRIDYN simulation data across the range of doses. However, the Cu isotopes present a clear variation between the measured and predicted ion profile for the implanted dose. The TOF-SIMS data close to the surface show a relatively lower concentration in Cu content than the peak concentration, which is consistent between both isotopes and is not seen in the TRIDYN simulation data. This is possibly due to a latency in the SIMS ionization of the sputtered material, which requires a build-up of the analysis beam deposition into a substrate prior to sufficient sputtering and ionization (steady-state regime). Though this is common in other SIMS sources, like Cs and O, for example, further investigations would be required to determine the degree of a steady-state latency with a C_{60} source as used in the TOF-SIMS for Figure 9a–d.

A similar ToF-SIMS analysis was performed to analyze $5 \times 5\,\mu m^2$ square areas where Ge^+ and Mn^+ isotopes had been implanted into intrinsic Si at 25 kV with a dose of 1×10^{15} ions cm^{-2} (Figure 9d). The C_{60} ToF-SIMS beam for this analysis was rastered over a $100 \times 100\,\mu m^2$ area, with a beam dose 1.93×10^{13} ions cm^{-2} for each layer, a lateral step resolution of 780 nm, and an approximate beam size of 1.5 μm. As with the Cu and Nd isotopes, the Ge and Mn implantations are well separated, with no evident mixing of the isotopes to a significant degree beyond that due to the wide-tail nature of the LMAIS Gaussian.

To further confirm the isotopic purity of the P-NAME ion beam, nanoSIMS analysis of a ^{70}Ge implanted region ($5 \times 5\,\mu m^2$, at 25 kV and 5.8×10^{14} ions cm^{-2} dose) was undertaken. The nanoSIMS instrument employed a Cs^+ analysis beam at 16 kV accelerating voltage, with a beam current of 0.45 pA. The raster field was set to $10 \times 10\,\mu m^2$ with 256×256 pixels, resulting in a beam step of approximately 39 nm. A dwell time of 500 μs per pixel was used, resulting in a dose of 9.2×10^{13} Cs^+ ions cm^{-2} for each of the 500 planes that

© 2023 The Authors. Advanced Engineering Materials published by Wiley-VCH GmbH

15272648, 0, Downloaded from https://onlinelibrary.wiley.com/doi/10.1002/adem.202300889 by Imperial College London, Wiley Online Library on [29/09/2023]. See the Terms and Conditions (https://onlinelibrary.wiley.com/terms-and-conditions) on Wiley Online Library for rules of use; OA articles are governed by the applicable Creative Commons License

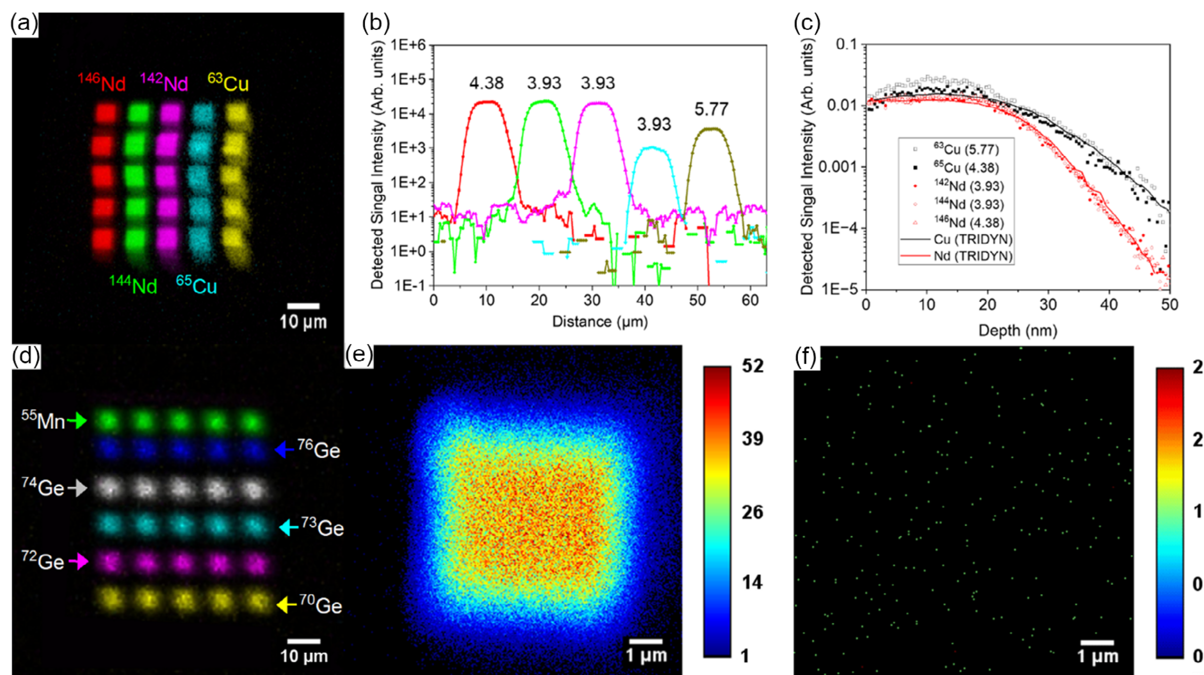

Figure 9. Secondary ion mass spectroscopy of various ion species implanted into intrinsic silicon. a) ToF-SIMS false-color image of isotopes of Cu and Nd (red—^{146}Nd, green—^{144}Nd, pink—^{142}Nd, blue—^{65}Cu, yellow—^{63}Cu). b) Line profiles of the top set of Cu and Nd squares. c) Depth profile of Cu and Nd from ToF-SIMS, depth calibrated using atomic force microscopy (Figure S4, Supporting Information). TRIDYN was used to simulate the depth distribution of the implantations and outputs a prediction in with good agreement with the experimental data. Doses are provided above each trace in (b) (and the legend of (c)) in units of $\times 10^{16}$ ions cm^{-2}. d) ToF-SIMS false-color image of isotopes of Ge and Mn (green—^{55}Mn, blue—^{76}Ge, gray—^{74}Ge, blue—^{73}Ge, pink—^{72}Ge, yellow—^{70}Ge). e) NanoSIMS false-color image of ^{70}Ge implanted into Si, with f) showing the same region analyzed by nanoSIMS, detecting no presence of ^{72}Ge (counts visible here constitute detector noise). Color scale in (e) and (f) indicate integrated counts per pixel in the associated datastack image.

comprise the datastacks for ^{70}Ge$^-$ and ^{72}Ge$^-$, shown in Figure 9e,f, respectively. The color scale bars in Figure 9e,f indicate the integrated counts for a given pixel (sum of signals for counts for that pixel across all planes). To ensure accurate detection, standard samples of pure Si and Ge were used for detector alignment, with a mass resolving power ($R = m/\Delta m$) for the nanoSIMS instrument >6000. Slit positions, specifically D1-4 (150 µm in diameter), ES-3 (30 µm width), and AS-2 (200 µm width), were employed. A double focusing mass spectrometer was utilized, and a total of 7 detectors were set up to capture signals for ^{70}Ge$^-$, ^{72}Ge$^-$, ^{12}C$^-$, ^{16}O$^-$, ^{29}Si$^-$, $(^{16}O)_2^-$, and $(^{28}Si)_2^-$. Further datastacks can be found in the Supporting Information, Figure S5. The analysis reveals that only ^{70}Ge is present within the doped region, with only dark-counts observed on the ^{72}Ge detector throughout the analysis.

6. Conclusion

The work presented here introduces the P-NAME FIB ion implantation system, with examples of high-resolution (<10 nm) ion beam imaging and direct-writing functionality of the ion beam in maskless lithographic applications. Secondary electron detector signals resulting from low dose ion implantation are also presented, as well as a demonstration of nondeterministic single ion implantation of Sb into 20 nm Si TEM membrane. The isotopic purity of the ion mass separation using a 50 µm mass resolving aperture is shown, with mass spectra of all readily available ion species provided. SIMS analysis of Mn, Cu, Ge, and Nd isotopic doping of intrinsic Si is presented to validate performance, with TRIDYN simulations of Cu and Nd into Si showing strong agreement with experimental data. This work demonstrates the suitability of a 50 µm aperture to provide isotopic resolution for a variety of species with high and low masses, though smaller apertures may be used (at the cost of a reduction in beam current) where a greater mass resolution is required.

The capability of isotopically pure implantation along with the extensive array of ion species available, the high spatial resolution of implantation, and direct writing functionality, provides a versatile system for site-specific ion implantation. The inclusion of a scanning electron microscope further extends the capabilities of the P-NAME tool into ion implantation of prefabricated devices with nondestructive imaging and preimplantation site location prior to any ion beam exposure. The capability of high frequency ion beam pulsing and secondary electron detection for ion implantation primes the P-NAME system to deliver isotopically pure single ion implantation with sub-10 nm accuracy across a variety of ion species. This is a vital capability in a number of applications for next generation technologies and facilitates the rapid prototyping of devices and nanoscale materials.

© 2023 The Authors. Advanced Engineering Materials published by Wiley-VCH GmbH

15272648, 0, Downloaded from https://onlinelibrary.wiley.com/doi/10.1002/adem.202300889 by Imperial College London, Wiley Online Library on [29/09/2023]. See the Terms and Conditions (https://onlinelibrary.wiley.com/terms-and-conditions) on Wiley Online Library for rules of use; OA articles are governed by the applicable Creative Commons License

7. Experimental Section

The P-NAME system was manufactured by Ionoptika Ltd. and fitted with an Orsay Eclipse Plus secondary electron microscope. The use and capabilities of the P-NAME system are fully described within the text of this article. The secondary electron image produced by the ion beam was subject to 80/20 knife-edge measurement to obtain a value for beam spot-size. This measurement was performed using an ImageJ GaussFit plugin, based on the electron beam imaging standard ASTM E986-9731. The tin nanosphere standard imaged was obtained from Agar Scientific (AGS1937T).

The PMMA resist used for the ion beam lithography exposures was Kayaku 495 PMMA 3A (3% in anisole), spun onto the polished silicon at 3500 rpm for 60 s, with an acceleration time of 1 s and a deceleration time of 2 s (SCS G3 Series spin-coater). Following the spin coating, the samples were subject to a bake at 150 °C for 5 min to evaporate any remaining solvent. The doses for specific exposures are described in text.

The HAADF-STEM images of Sb ions into a Si membrane were obtained with a probe-corrected Thermo Fisher Scientific Titan G2 80-200 S/TEM, operating at an accelerating voltage of 200 kV. The images were acquired using a semiconvergence angle of 21 mrad and HAADF inner collection angle of 54 mrad.

The ion beam mass spectra were obtained by measuring the ion beam current in the Faraday cup of the sample chamber of the system as a function of varying Wien filter electrostatic plate voltage. This varied the mass selected (as per Equation (1)) with a tunability described in the text. The beam current was measured using the P-NAME system's internal current measurement systems and a Keithley 6485 picoammeter where a more sensitive current measurement was required to achieve a good signal-to-noise ratio (namely, for Si^{+}, Si^{2+}, Sb^{+}, Sb^{2+}, In^{2+}, B^{+}).

The mass-resolution figures of the isotopic mass spectra shown in Figure 7 were obtained by fitting the current measurement data as a function of mass, calibrated from Wien filter voltage (or time using a constant if the picoammeter was used to measure the current), with a Gaussian function. OriginPro 2022b data analysis software was used to perform the GaussAmp nonlinear curve fit, with a chi-squared minimization used to optimize the fit. The fitting parameters of note that were obtained were the FWHM, the peak position, and the integrated area under the peak. The area for each peak was used to determine the relative percentage area of a given isotope against the rest of the isotopes in that spectra (for a given ionization state), as shown in Figure 8 and tabulated in Table S1, Supporting Information.

A similar method was employed in order to estimate the literature mass-resolution figures. First, the spectra presented in the associated reference were subject to digitization (using the OriginPro 2022b Digitizer function); the digitized data were then converted to be a function mass rather than voltage (or magnetic field) variation, as reported. The aforementioned fitting procedure was then applied, with FWHM and peak position values being used to estimate the mass-resolution figure where required (Table 1). It is important to note that the digitization technique is not expected to be an exact replication of the data which was reported and relies on the quality of the figure presented in the associated reference. For this reason, the values presented in Table 1 are taken to be indicative only and, where possible, mass-resolution values quoted in the reference are used instead.

The samples prepared for isotopic mass-resolution verification were implanted using the P-NAME system, with doses and specific isotopes described within the text. The ToF-SIMS analysis was performed using a J105 3D Chemical Imager (Ionoptika, UK), with additional SIMS analysis performed using a NanoSIMS 50L (Cameca, France); the detection parameters for both of these systems are described within the main text. For the nanoSIMS experiment, an ImageJ OpenMIMS plugin (Harvard University, Cambridge, MA, USA) was utilized for data analysis. A nanoSURF Core AFM was utilized for postlithography imaging and ToF-SIMS analysis depth calibration.

Simulations of Cu and Nd implantation into Si for the purposes of comparison to ToF-SIMS depth-profile results were performed using the 2020 Linux build of the TRIDYN code. The simulation parameters used were 25 keV and 3° beam offset, to match experimental conditions, and a simulated thickness of 1000 Å with 100 depth intervals (bin depth of 10 Å). The precision value used for both simulations was 0.0001. The maximum relative change of layer areal density per pseudoprojectile (the indicative parameter for statistical validity of a simulation, required to be $<1\%$) was 0.69% and 0.72% for the Cu and Nd simulations, respectively.

Supporting Information

Supporting Information is available from the Wiley Online Library or from the author.

Acknowledgements

This work was supported by the EPSRC (grant nos. EP/R025576/1, EP/V001914/1, and EP/R00661X/1) (Henry Royce Institute) and by capital investment by the University of Manchester. S.J.H acknowledges the European Research Council under the European Union's Horizon 2020 research and innovation program (grant agreement no. 715502, EvoluTEM). Electron microscopy access was supported by the Henry Royce Institute for Advanced Materials, funded through EPSRC (grant nos. EP/R00661X/1, EP/S019367/1, EP/P025021/1, EP/P025498/1, and EP/S021531/1).

Conflict of Interest

As per submitted paper is not included here (AB and GA were employed by Ionoptika, the manufacturer of the system this paper describes).

Data Availability Statement

The data that support the findings of this study are available from the corresponding author upon reasonable request.

Keywords

focused ion beam, high-resolution isotopic doping, nanomaterials engineering, nanoscale implantation, nanoscale lithography

Received: June 12, 2023
Revised: August 24, 2023
Published online:

[1] J. M. Poate, K. Saadatmand, *Rev. Sci. Instrum.* **2002**, *73*, 868.
[2] P. Li, S. Chen, H. Dai, Z. Yang, Z. Chen, Y. Wang, Y. Chen, W. Peng, W. Shan, H. Duan, *Nanoscale* **2021**, *13*, 1529.
[3] V. Garg, R. G. Mote, J. Fu, *Adv. Mater. Technol.* **2018**, *3*, 1800100.
[4] E. Chason, S. T. Picraux, J. M. Poate, J. O. Borland, M. I. Current, T. Diaz De La Rubia, D. J. Eaglesham, O. W. Holland, M. E. Law, C. W. Magee, J. W. Mayer, J. Melngailis, A. F. Tasch, *J. Appl. Phys.* **1997**, *81*, 6513.
[5] L. Bruchhaus, P. Mazarov, L. Bischoff, J. Gierak, A. D. Wieck, H. Hövel, *Appl. Phys. Rev.* **2017**, *4*, 011302.
[6] K. Keskinbora, C. Grevent, U. Eigenthaler, M. Weigand, G. Schutz, *ACS Nano* **2013**, *7*, 9788.
[7] W. R. McGehee, E. Strelcov, V. P. Oleshko, C. Soles, N. B. Zhitenev, J. J. McClelland, *ACS Nano* **2019**, *13*, 8012.
[8] Y. Chen, K. Bi, Q. Wang, M. Zheng, Q. Liu, Y. Han, J. Yang, S. Chang, G. Zhang, H. Duan, *ACS Nano* **2016**, *10*, 11228.

© 2023 The Authors. Advanced Engineering Materials published by Wiley-VCH GmbH

15272648, 0, Downloaded from https://onlinelibrary.wiley.com/doi/10.1002/adem.202300889 by Imperial College London, Wiley Online Library on [29/09/2023]. See the Terms and Conditions (https://onlinelibrary.wiley.com/terms-and-conditions) on Wiley Online Library for rules of use; OA articles are governed by the applicable Creative Commons License

[9] K. Groot-Berning, T. Kornher, G. Jacob, F. Stopp, S. T. Dawkins, R. Kolesov, J. Wrachtrup, K. Singer, F. Schmidt-Kaler, *Phys. Rev. Lett.* **2019**, *123*, 106802.
[10] B. N. Murdin, N. Cassidy, D. Cox, R. Webb, R. J. Curry, *Phys. Status Solidi B* **2021**, *258*, 2000615.
[11] M. Hollenbach, N. Klingner, N. S. Jagtap, L. Bischoff, C. Fowley, U. Kentsch, G. Hlawacek, A. Erbe, N. V. Abrosimov, M. Helm, Y. Berencén, G. V. Astakhov, *Nat. Commun.* **2022**, *13*, 7683.
[12] M. Hori, T. Shinada, K. Taira, N. Shimamoto, T. Tanii, T. Endo, I. Ohdomari, *Nanotechnology* **2009**, *20*, 365205.
[13] T. Shinada, S. Okamoto, T. Kobayashi, I. Ohdomari, *Nature* **2005**, *437*, 1128.
[14] N. Klingner, G. Hlawacek, P. Mazarov, W. Pilz, F. Meyer, L. Bischoff, *Beilstein J. Nanotechnol.* **2020**, *11*, 1742.
[15] T. Matsukawa, T. Fukai, S. Suzuki, K. Hara, M. Koh, I. Ohdomari, *Appl. Surf. Sci.* **1997**, *117–118*, 677.
[16] T. Hopf, D. N. Jamieson, S. M. Hearne, C. Yang, C. I. Pakes, A. S. Dzurak, E. Gauja, R. G. Clark, *Nucl. Instrum. Methods Phys. Res. Sect. B* **2005**, *231*, 463.
[17] J. A. Seamons, E. Bielejec, M. S. Carroll, K. D. Childs, *Appl. Phys. Lett.* **2008**, *93*, 043124.
[18] V. Chandrasekaran, M. Titze, A. R. Flores, D. Campbell, J. Henshaw, A. C. Jones, E. S. Bielejec, H. Htoon, *Adv. Sci.* **2023**, *10*, e2300190.
[19] T. S. Shinada, A. I. Ishikawa, M. F. Fujita, K. Y. Yamashita, I. O. Ohdomari, *Jpn. J. Appl. Phys.* **1999**, *38*, 3419.
[20] L. Bischoff, P. Mazarov, L. Bruchhaus, J. Gierak, *Appl. Phys. Rev.* **2016**, *3*, 021101.
[21] J. L. Pacheco, M. Singh, D. L. Perry, J. R. Wendt, G. Ten Eyck, R. P. Manginell, T. Pluym, D. R. Luhman, M. P. Lilly, M. S. Carroll, E. Bielejec, *Rev. Sci. Instrum.* **2017**, *88*, 123301.
[22] A. M. Jakob, S. G. Robson, V. Schmitt, V. Mourik, M. Posselt, D. Spemann, B. C. Johnson, H. R. Firgau, E. Mayes, J. C. Mccallum, A. Morello, D. N. Jamieson, *Adv. Mater.* **2022**, *34*, e2103235.
[23] T. Schenkel, J. A. Liddle, A. Persaud, A. M. Tyryshkin, S. A. Lyon, R. De Sousa, K. B. Whaley, J. Bokor, J. Shangkuan, I. Chakarov, *Appl. Phys. Lett.* **2006**, *88*, 112101.
[24] R. Debroux, C. P. Michaels, C. M. Purser, N. Wan, M. E. Trusheim, J. Arjona Martínez, R. A. Parker, A. M. Stramma, K. C. Chen, L. De Santis, E. M. Alexeev, A. C. Ferrari, D. Englund, D. A. Gangloff, M. Atatüre, *Phys. Rev. X* **2021**, *11*, 041041.
[25] S. Lagomarsino, A. M. Flatae, H. Kambalathmana, F. Sledz, L. Hunold, N. Soltani, P. Reuschel, S. Sciortino, N. Gelli, M. Massi, C. Czelusniak, L. Giuntini, M. Agio, *Front. Phys.* **2021**, *8*, 601362.
[26] K. Groot-Berning, G. Jacob, C. Osterkamp, F. Jelezko, F. Schmidt-Kaler, *New J. Phys.* **2021**, *23*, 063067.
[27] M. Fischer, J. M. Caridad, A. Sajid, S. Ghaderzadeh, M. Ghorbani-Asl, L. Gammelgaard, P. Bøggild, K. S. Thygesen, A. V. Krasheninnikov, S. Xiao, M. Wubs, N. Stenger, *Sci. Adv.* **2021**, *7*, eabe7138.
[28] M. Kianinia, S. White, J. E. Fröch, C. Bradac, I. Aharonovich, *ACS Photonics* **2020**, *7*, 2147.
[29] S. P. Pavunny, A. L. Yeats, H. B. Banks, E. Bielejec, R. L. Myers-Ward, M. T. Dejarld, A. S. Bracker, D. K. Gaskill, S. G. Carter, *Sci. Rep.* **2021**, *11*, 3561.
[30] Y. Song, Z. Xu, R. Li, H. Wang, Y. Fan, M. Rommel, J. Liu, G. V. Astakhov, G. Hlawacek, B. Li, J. Xu, F. Fang, *Nanomanuf. Metrol.* **2020**, *3*, 205.
[31] S. Wang, L. Yang, R. Cheng, Y. Xu, M. Shen, R. L. Cone, C. W. Thiel, H. X. Tang, *Appl. Phys. Lett.* **2020**, *116*, 151103.
[32] W. Möller, W. Eckstein, J. P. Biersack, *Comput. Phys. Commun.* **1988**, *51*, 355.
[33] N. S. Smith, J. A. Notte, A. V. Steele, *MRS Bull.* **2014**, *39*, 329.
[34] B. S. Cho, H. J. Oh, H. S. Uhm, S. O. Kang, C. Kim, Y. Choi, E. H. Choi, *Curr. Appl. Phys.* **2011**, *11*, S172.
[35] Y. Zheng, H. Wang, S. Hou, D. Xia, *Adv. Mater. Technol.* **2017**, *2*, 1600237.
[36] H. S. Khaliq, A. Nauman, J. W. Lee, H. R. Kim, *Adv. Opt. Mater.* **2023**, *11*, 2300644.
[37] N. Cassidy, P. Blenkinsopp, I. Brown, R. J. Curry, B. N. Murdin, R. Webb, D. Cox, *Phys. Status Solidi A* **2020**, *218*, 2000237.
[38] S. Bauerdick, L. Bruchhaus, P. Mazarov, A. Nadzeyka, R. Jede, J. Fridmann, J. E. Sanabia, B. Gila, B. R. Appleton, *J. Vac. Sci. Technol. B Nanotechnol. Microelectron.* **2013**, *31*, 06F404.
[39] B. Gila, B. R. Appleton, J. Fridmann, P. Mazarov, J. E. Sanabia, S. Bauerdick, L. Bruchhaus, R. Mimura, R. Jede, *AIP Conf. Proc.* ***2011***, *1336*, 243.
[40] C. Aidinis, *Microelectron. Eng.* **2004**, *73–74*, 116.
[41] L. Bischoff, W. Pilz, T. Ganetsos, C. Akhmadaliev, C. J. Aidinis, C. A. Londos, *J. Phys. Conf. Ser.* **2005**, *10*, 214.
[42] L. Bischoff, G. L. Mair, C. J. Aidinis, C. A. Londos, C. Akhmadaliev, T. Ganetsos, *Ultramicroscopy* **2004**, *100*, 1.
[43] F. Machalett, R. Muhle, *J. Phys. D: Appl. Phys.* **1994**, *27*, 1286.
[44] K. Umemura, T. Ishitani, H. Tamura, *Jpn. J. Appl. Phys.* **1986**, *25*, L885.
[45] T. Ganetsos, G. L. R. Mair, C. J. Aidinis, L. Bischoff, *Physica B* **2003**, *340–342*, 1166.
[46] L. Bischoff, W. Pilz, P. Mazarov, A. D. Wieck, *Appl. Phys. A* **2010**, *99*, 145.
[47] P. Mazarov, A. Melnikov, R. Wernhardt, A. D. Wieck, *Appl. Surf. Sci.* **2008**, *254*, 7401.
[48] J. R. de Laeter, J. K. Böhlke, P. De Bièvre, H. Hidaka, H. S. Peiser, K. J. R. Rosman, P. D. P. Taylor, *Pure Appl. Chem.* **2003**, *75*, 683.
[49] S. Tan, R. Livengood, Y. Greenzweig, Y. Drezner, D. Shima, *J. Vac. Sci. Technol. B, Nanotechnol. Microelectron.* **2012**, *30*, 06F606.
[50] M. Titze, J. L. Pacheco, T. Byers, S. B. Van Deusen, D. L. Perry, D. Weathers, E. S. Bielejec, *J. Vac. Sci. Technol. A* **2021**, *39*, 063222.

© 2023 The Authors. Advanced Engineering Materials published by Wiley-VCH GmbH

15272648, 0, Downloaded from https://onlinelibrary.wiley.com/doi/10.1002/adem.202300889 by Imperial College London, Wiley Online Library on [29/09/2023]. See the Terms and Conditions (https://onlinelibrary.wiley.com/terms-and-conditions) on Wiley Online Library for rules of use; OA articles are governed by the applicable Creative Commons License